# DAP: A Discrete-token Autoregressive Planner for Autonomous Driving

Bowen Ye<sup>1,3</sup> Bin Zhang<sup>1</sup> Hang Zhao\*,1,2 <sup>1</sup>Shanghai Qi Zhi Institute <sup>2</sup>IIIS, Tsinghua University <sup>3</sup>Shanghai Jiaotong University = MSE or NLL Cross Entropy routing tokens Trajectory Decoder **Decoder-only** Transformer tokens 吞 Scene Encoder **Tokens** traj tokens Routing BEV Traj Routing **BEV** Traj a): Action Planning Models b):Decoder-only Autoregressive Model

Figure 1. Comparison of planning architectures. (a) Non-autoregressive direct mapping: encode historical observations to continuous embeddings and decode future trajectories in one forward pass. (b) DAP (ours): a *discrete-token* autoregressive planner that *jointly* forecasts future environment representations and ego trajectories, producing aligned supervision and sampling-based rollouts that improve planning quality and robustness.

#### **Abstract**

Gaining sustainable performance improvement with scaling data and model budget remains a pivotal yet unresolved challenge in autonomous driving. While autoregressive models exhibited promising data-scaling efficiency in planning tasks, predicting ego trajectories alone suffers sparse supervision and weakly constrains how scene evolution should shape ego motion. Therefore, we introduce DAP, a discrete-token autoregressive planner that jointly forecasts BEV semantics and ego trajectories, thereby enforcing comprehensive representation learning and allowing predicted dynamics to directly condition ego motion. In addition, we incorporate a reinforcement-learning-based finetuning, which preserves supervised behavior cloning priors while injecting reward-guided improvements. Despite a compact 160M parameter budget, DAP achieves stateof-the-art performance on open-loop metrics and delivers competitive closed-loop results on the NAVSIM benchmark. Overall, the fully discrete-token autoregressive formulation operating on both rasterized BEV and ego actions provides a compact yet scalable planning paradigm for autonomous driving.

## 1. Introduction

Research on autonomous driving planning can be categorized, from a temporal modeling perspective, into two paradigms: *autoregressive* (*AR*) approaches that causally decode the ego's actions one step at a time [11, 14, 48] and *non-AR approaches* that generate the entire future trajectory in a single forward pass. The latter encompasses methods ranging from end-to-end predictive methods [19, 28] that directly map sensor data to ego actions following certain command queries, to diffusion-based generative methods [18, 29] that model the distribution of ego trajectories conditioned on sensor data and generate planning trajectories through sampling and iterative refinement. Although non-AR methods have been extensively studied, AR approaches are gaining increasing attention in recent research [34, 45], mainly because of their superior potential for scaling up.

Recent results on large language models show that *decoder-only* Transformers trained as next-token predictors over discrete text tokens scale efficiently with data, model size, and compute budget, which exhibits a predictable power-law trend [12, 20]. Meanwhile, the scaling laws of autonomous driving have also been reported, with studies showing that both open- and *closed-loop* metrics improve with training compute and the compute-optimal balances between model and data size have also been char-

<sup>(\*)</sup> Corresponding author.

acterized [1]. Building on this, DriveVLA-W0 argues that, under a comparable resource budget, *autoregressive* planners scale more efficiently than other query-based or diffusion-based counterparts [25]. Guided by this evidence, we cast motion forecasting and planning as a discrete-token sequence modeling task and address it using a **decoder-only** Transformer with a pre-defined tokenization scheme, to thereby leverage the favorable scaling law of such architecture and ground progress in rigorous closed-loop evaluation and a compute-centric development roadmap.

Nevertheless, scaling alone does not remedy the supervision sparsity, which is an issue that constrains the performance of previous models without explicit world modeling capacity. To fill this gap within our discrete-token, decoderonly framework, we incorporate a world-modeling-style objective [4, 23, 24]: the model *jointly* predicts future semantic BEV representations of environment and discrete  $\kappa$ -a (curvature and acceleration) trajectory tokens of ego at every step. By jointly forecasting BEV semantics and future trajectories, we provide dense spatio-temporal supervision, per-cell BEV constraints at every step together with explicit kinematic targets. This couples scene evolution with ego motion in the latent state and improves multi-step credit assignment beyond sparse waypoint labels.

As shown in Figure 1, our model first tokenizes historical BEV context with a VO-VAE [40] to obtain discrete environment tokens. These tokens, combined with discretized  $\kappa$ -a trajectory tokens from the past, are fed into an autoregressive transformer that decodes a sequence of future tokens. At each step, the decoder jointly predicts (i) nextstep semantic BEV states tokens that summarize near-future scene evolution and (ii)  $\kappa$ -a trajectory tokens that govern ego motion, thereby tightly coupling scene understanding with motion generation under dense, spatio-temporally aligned supervision. The discrete token interface stabilizes module interactions and enables efficient token-level rollouts at inference. In contrast to the left-hand baseline, which maps history directly to future trajectories in a single pass, our approach forecasts the evolving environment and the trajectory in an interleaved manner, thereby improving robustness under closed-loop execution.

Following this design, we find that pure imitation learning (IL), though tends to fit ground-truth trajectories well, can only weakly couple ego planning with predicted scene evolution, leading to ego trajectories that interact only loosely with the surrounding scene dynamics. To address this, we adopt SAC-BC (soft-actor-critic plus behavior-cloning) [30] fine-tuning, which preserves behavior-cloning priors yet reinforces them by leveraging reward signals so that future environment forecasting can more directly inform trajectory generation. It is proved that our model remains compact, achieves state-of-the-art results on openloop evaluation, and delivers strong closed-loop perfor-

mance on NavSim benchmark, despite the small parameter count. Our main contributions are as follows.

- Decoder-only autoregressive MoE with discrete tokens. We propose DAP, a discrete-token auto-regressive planner with decoder-only Transformer architecture and sparse MoE layers. The DAP generates discrete scene and trajectory tokens autoregressively, yielding a simple interface and efficient decoding.
- Joint environment-trajectory forecasting. DAP jointly predicts future environment representations (semantic BEV) and κ-a trajectory tokens, providing dense, spatiotemporally aligned supervision that couples scene understanding with motion generation.
- SAC-BC fine-tuning beyond pure IL. SAC-BC surpasses pure IL while preserving architectural simplicity, and it strengthens the coupling between predicted environment states and generated ego trajectories.
- **Compact yet strong performance.** With a small parameter budget, the model achieves *state-of-the-art* open-loop results and strong closed-loop results on NavSim.

## 2. Related Works

# 2.1. End-to-end Models in Autonomous Driving

End-to-end trajectory planning in autonomous driving has evolved from early perception-prediction-planning stacks to unified models that learn plans directly from multimodal inputs [5, 13, 38]. Within this landscape, two complementary design ideas have emerged. The first treats planning as autoregressive sequence modeling with Transformers, generating future states or trajectories step by step and, in recent large-model variants, operating on discrete tokens with GPT-style decoders [11, 14, 25, 48]. The second embraces world modeling, jointly forecasting scene evolution and ego motion to provide dense, time-aligned supervision that strengthens the coupling between environment prediction and plan generation [4, 23, 24]. These ideas are not opposed; recent systems such as DriveVLA-W0 [25] and UMGen [44] exemplify their combination by using discrete-token autoregression within a world-modeling context. However, these works target on pixel-level world models have to adopt heavy pretrained vision or visionlanguage models as their backbone. In contrast, our method focuses on world modeling in compact BEV-latent space, where discrete BEV-semantic tokens are predicted in a interleaved manner along with ego motion tokens. The advantage is that our method makes the system lighter and simpler to train, avoids tedious image rollouts and remains RLfriendly, while still providing planning-centric alignment and dense supervision.

## 2.2. Reinforcement learning for trajectory planning

Pure imitation learning (IL) often overfits to expert demonstrations, yielding trajectories that closely mimic the expert while under-attending to critical scene factors; under covariate shift or out-of-distribution (OOD) conditions, such policies are prone to compounding errors and risks of collisions. This limitation motivates the use of reinforcement learning (RL), which optimizes task-level objectives beyond trajectory matching. Proximal policy optimization (PPO)-style methods have been adopted to improve closedloop behavior, e.g., adversarial or preference-driven policy optimization such as APO [19] and earlier adversarial formulations [7], as well as GRPO-style updates [50] with precedents in general-purpose RL training [36]. Beyond pure RL, IL+RL hybrids combine supervised imitation losses with reward-driven objectives to balance stability and performance. Representative examples include SAC-BC [30], which augments behavior cloning with soft actor-critic updates, and [27]ReCogDrive's joint optimization of RL and BC terms ( $\mathcal{L}_{\rm RL} + \mathcal{L}_{\rm BC}$ ) to couple languageconditioned reasoning with planning.

#### 2.3. Trajectory Post-tuning

Many systems refine planner outputs with post-tuning for safety and comfort, using either rule-based safety layers or lightweight optimization. Representative approaches include safety shields that detect violations and trigger conservative fallbacks [41], and smoothing via convexified collision/kinematic constraints to improve clearance and ride comfort [33]. We follow this practice with a minimal posttuning module that attenuates lateral jitter and jerk while preserving feasibility, serving as a constraint-aware polish rather than a second planner [35].

#### 3. Methodology

In this section, we propose DAP, in which scene understanding is aligned with motion generation through three components: (i) A discrete-token, decoder-only autoregressive transformer with sparse MoE routing jointly forecasts future semantic BEV states and  $\kappa$ -a trajectory tokens, providing dense, spatio-temporally aligned supervision. (ii) A SAC-BC-based offline RL stage fine-tunes the planner beyond pure imitation learning, leveraging reward signals to strengthen the coupling between predicted environment evolution and trajectory decisions while preserving architectural simplicity. (iii) A lightweight trajectory post-tuning step applies rule-based checks to improve ride comfort and reduce lateral deviation without modifying the planner or its discrete interface. Together, these components yield a compact and efficient pipeline that maintains end-to-end inference while enhancing closed-loop robustness.

#### 3.1. Model Structure

We adopt a planning model that maps a high-level command, recent camera-LiDAR observations, and the ego history to a sequence of future BEV-semantic and trajectory tokens. A perception module fuses the multimodal streams into BEV features and discretizes them as environment tokens. A decoder-only, autoregressive Transformer with sparse MoE then conditions on the command, the environment tokens, and past trajectory tokens to jointly decode future BEV and trajectory tokens across the prediction horizon (Fig. 2). The sparse MoE design expands the planner's capacity and allows different experts to specialize on diverse traffic patterns and scene configurations, improving robustness across scenarios without incurring prohibitive inference cost. This formulation provides a fully discrete, time-aligned interface in which scene dynamics and ego motion are learned within a single sequence, supporting dense supervision and clean scaling.

a) Input Tokenization. We discretize three modalities with separate, modality-aware quantization schemes.

**Command:** We treat the high-level command as a categorical variable. Let  $c \in \{1, \dots, C\}$  denote the command class. We convert c into a one-hot vector  $\mathbf{o} \in \{0, 1\}^C$ .

BEV feature: We fuse multi-modal observations into a semantic BEV feature map  $\mathbf{F} \in \mathbb{R}^{H \times W \times D}$ , and quantize it using a trained VQ-VAE. The encoder  ${\cal E}$  produces a latent grid  $\mathbf{Z} = E(\mathbf{F}) \in \mathbb{R}^{h \times w \times d}$ . Given a codebook  $\mathcal{E} = \{\mathbf{e}_k\}_{k=1}^K$ ,  $\mathbf{e}_k \in \mathbb{R}^d$ , each latent vector  $\mathbf{z}_{i,j}$  is vector-quantized by nearest neighbor:

$$k^{\star}(i,j) = \arg\min_{k \in \{1,\dots,K\}} \|\mathbf{z}_{i,j} - \mathbf{e}_k\|_2^2$$
 (1)

The BEV tokens are the codebook indices  $\{k^*(i,j)\}$  laid out over the latent grid.

**Ego states:** Given ego states  $\{(x_t, y_t, \psi_t)\}_{t=0}^T$  sampled with interval  $\Delta t$ , we convert positions and yaw to curvatureacceleration  $(\kappa_t, a_t)$  and then discretize them with an uniform grid. The transformation from  $(x_t, y_t, \psi_t)_{t=0}^n$  to  $(\kappa_t, a_t)_{t=0}^n$  is defined as follows:

$$v_t = \frac{\sqrt{(x_{t+1} - x_t)^2 + (y_{t+1} - y_t)^2}}{\Delta t}$$
 (2a)

$$\omega_t = \frac{\operatorname{wrap}(\psi_{t+1} - \psi_t)}{\Delta t} \tag{2b}$$

$$\omega_t = \frac{\operatorname{wrap}(\psi_{t+1} - \psi_t)}{\Delta t}$$

$$\kappa_t = \frac{\omega_t}{\max(v_t, \varepsilon)}$$
(2b)

$$a_t = \frac{v_{t+1} - v_t}{\Delta t} \tag{2d}$$

where  $\varepsilon > 0$  avoids division by zero (and wrap(·) unwraps yaw to  $(-\pi, \pi]$ ). And then  $(\kappa_t, a_t)_{t=0}^n$  are discretized into token indices  $(i_t^{\kappa}, i_t^a)_{t=0}^n$  by uniform grid. We optionally pack them into a single trajectory token:

$$S_t = i_t^{\kappa} \cdot A + i_t^a \in \{0, \dots, AK - 1\}.$$
 (3)

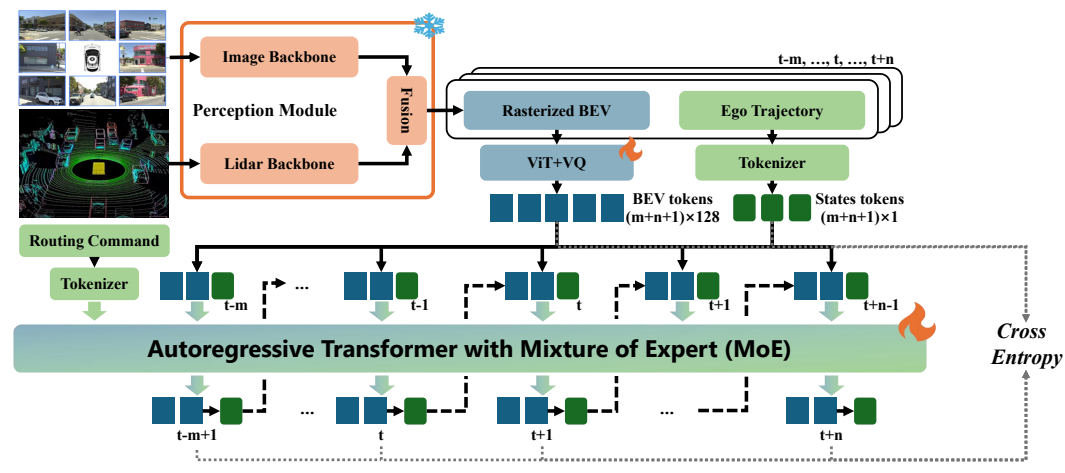


Figure 2. Overall architecture of **DAP**. Historical multi-modal inputs are tokenized (VQVAE for BEV,  $\kappa$ –a discretization for ego actions), then a decoder-only autoregressive Transformer with sparse MoE jointly predicts future BEV and ego trajectory tokens. The joint forecasting provides dense, time-aligned signals that couple scene evolution with motion generation.

where A and K are the total numbers of acceleration and curvature bins, respectively.

b) Autoregressive Planning Transformer. We concatenate multimodal chunks over a history of H steps following [42], and the sequence begins with one command token  $C_{t^*}$  where the current time step is  $t^*$ , and for each time step  $t = t^* - H, \ldots, t^*$  we append BEV tokens  $V_t$  followed by one trajectory token  $A_t$ :

$$\mathbf{z_{t^*-H,t^*}} = [C_{t^*}, V_{t^*-H}, A_{t^*-H}, \dots, V_{t^*}, A_{t^*}].$$

where  $V_t \equiv [V_{t,1}, \dots, V_{t,M}]$  contains M BEV tokens at step t. All tokens are mapped into a shared embedding space and fed to a decoder-only Transformer, which maintains a causal state over the prefix  $\mathbf{z}_{< p}$  at each position p.

Given the observed context  $\mathbf{z}_{\leq t}$ , the Transformer predicts the next-step tokens in a causal manner. At each future step t+1, BEV tokens are first generated sequentially, followed by one trajectory token:

$$p_{\theta}(V_{t+1,m} \mid \mathbf{z}_{\leq t}, V_{t+1, \leq m}) = \operatorname{softmax}(W_{\text{out}} h_{t+1, m-1}),$$

$$m = 1, \dots, M \qquad (4a)$$

$$p_{\theta}(A_{t+1} \mid \mathbf{z}_{\leq t}, V_{t+1,1:M}) = \operatorname{softmax}(W_{\text{out}} h_{t+1,M})$$
 (4b)

where  $h_{t+1,m-1}$  and  $h_{t+1,M}$  denote the hidden states before emitting  $V_{t+1,m}$  and  $A_{t+1}$ , respectively. A shared output projection  $W_{\text{out}} \in \mathbb{R}^{V_{\text{all}} \times d}$  corresponds to a unified discrete codebook of size  $V_{\text{all}}$ , within which disjoint index ranges are reserved for command, BEV and trajectory tokens. This unified formulation enables consistent cross-modality modeling, while the generation order (BEV first, then trajectory) allows motion prediction to explicitly condition on the newly decoded scene representation.

c) Training and Inference. Given ground-truth sequences  $\mathbf{z}_{1:T}$ , the model is optimized to maximize the log-likelihood of next-step predictions conditioned on either

ground-truth or previously generated tokens:

$$\mathcal{L}_{AR} = -\sum_{t=1}^{T} \log p_{\theta}(\mathbf{z}_{t} \mid \tilde{\mathbf{z}}_{< t})$$
 (5a)

$$\tilde{\mathbf{z}}_{< t} = (1 - p) \times \mathbf{z}_{< t} + p \times \hat{\mathbf{z}}_{< t}$$
 (5b)

where  $\hat{\mathbf{z}}_{< t}$  denotes the tokens predicted by the model, and p is the sampling ratio between ground-truth and predicted tokens. Under pure teacher forcing, p=0, while during scheduled sampling, p is gradually increased from 0 to 1, approaching the inference behavior. We adopted the latter during the training process, which allows the Transformer to learn from oracle supervision while progressively adapting to its own prediction distribution.

At each decoding step, the Transformer produces logits for the trajectory token  $S_t$  and the BEV tokens  $V_t$ . We train with a weighted sum of cross-entropy losses applied separately to the two heads, yielding the overall objective.

$$\mathcal{L}_{\text{bev}} = -\sum_{t=0}^{T} \sum_{m=1}^{M} \log p_{\theta}(V_{t,m} \mid \tilde{\mathbf{z}}_{< t}, V_{t,< m}),$$
 (6a)

$$\mathcal{L}_{\text{traj}} = -\sum_{t=0}^{T} \log p_{\theta}(A_t \mid \tilde{\mathbf{z}}_{< t}, V_t), \tag{6b}$$

where T denotes samples time horizon. The total loss is a weighted combination of the two terms:

$$\mathcal{L}_{\text{total}} = \lambda_{\text{trai}} \mathcal{L}_{\text{trai}} + \lambda_{\text{bev}} \mathcal{L}_{\text{bev}}$$

where  $\lambda_{traj}$  and  $\lambda_{bev}$  weight the trajectory and BEV losses, respectively. We use a larger  $\lambda_{traj}$  to prioritize motion accuracy and a smaller  $\lambda_{bev}$  to stabilize scene representation without dominating optimization. This asymmetric weighting produces a coherent BEV context that supports more accurate, physically plausible trajectories. The autoregressive

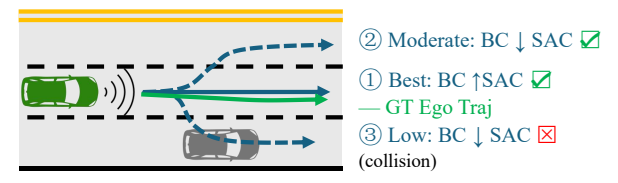


Figure 3. The necessity of RL: for the sub-optimal trajectories 2 and 3, though their BC losses are nearly identical, the 3rd one would yield a collision and hence get higher SAC loss.

design enforces temporal causality and inter-step consistency, capturing long-horizon dependencies and ego-scene interactions.

# 3.2. Reinforcement Learning(RL)

In multi-modal futures, the supervised objective (e.g., way-point MSE or cross-entropy over discrete  $\kappa-a$  / BEV to-kens) often treats several feasible continuations as loss-equivalent relative to the expert label. In the scene of Fig. 3, "drift left", and "drift right" can incur nearly identical surrogate loss, despite having distinct risk profiles (the left retains a larger safety buffer, while the right collides with another vehicle). This aleatoric ambiguity and the symmetry of the surrogate loss induce mode averaging or arbitrary mode selection, manifesting as lateral dithering or suboptimal lane choice with no incentive for safety margins, comfort, or time-to-collision.

Even with a denser objective that jointly reconstructs BEV and trajectory tokens, we mainly reduce imitation errors; the decision-theoretic ambiguity remains. The model can still match scene semantics yet select a riskier mode that is equivalent under the surrogate loss. IL also inherits dataset biases and is brittle under covariate shift. Once the policy leaves the expert manifold, supervision offers little corrective signal. We therefore adopt SAC-BC [30], which optimizes explicit rewards for safety, comfort, and progress while regularizing toward the BC prior. This breaks the loss symmetry, discourages hazardous modes, and preserves the discrete autoregressive interface.

**SAC-BC with trajectory-only actions.** The trajectory token  $A_t \in \{0,\dots,A-1\}$  is the only action. BEV tokens  $V_{t,1:M}$  are supervised and appear only in the causal prefix  $\operatorname{ctx}_t = [C_{t^*}, V_{t^*-H}, A_{t^*-H}, \dots, V_t, A_{t-1}]$ . Within each step the backbone predicts  $V_{t,1:M}$  and then the policy selects  $A_t$  from  $\pi_{\phi}(A_t \mid \operatorname{ctx}_t)$ .

**Reward signal.** Let  $d_{\rm ctr}(t)$  and  $d_{\rm clr}(t)$  denote the ego's distances (in meters) at step t to the lane centerline and to the nearest obstacle, respectively (measured in the BEV frame). We use bounded, scaled geometry rewards

$$r_{\text{ctr}}(t) = \left[1 - \frac{d_{\text{ctr}}(t)}{\sigma_{\text{ctr}}}\right]_{+}; r_{\text{clr}}(t) = \left[\frac{d_{\text{ctr}}(t)}{\sigma_{\text{clr}}}\right]_{+}; [x]_{+} = \max(x, 0).$$
 (7)

For comfort, we compute kinematics according to Eq. 2  $(v_t, a_t, \omega_t \text{ from } (x_t, y_t, \text{yaw}_t))$  and penalize acceleration variation and angular acceleration under a low-speed mask:

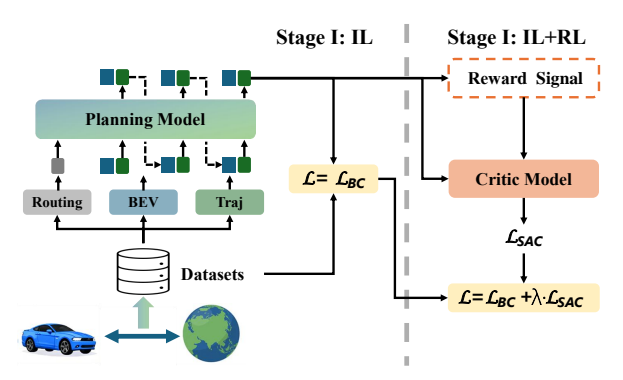


Figure 4. Two-stage training: (I) supervised pretraining with cross-entropy losses on trajectory and environment tokens, and (II) offline SAC-BC fine-tuning that augments the policy with reward-driven adaptation while retaining behavior consistency.

$$r_{\mathrm{comf}}(t) = -\left(\lambda_{\Delta a} |\Delta a_t| + \lambda_{\alpha} |\alpha_t|\right) \mathbf{1}\{|v_t| > \varepsilon_{\mathrm{spd}}\}.$$
 (8)

where  $\Delta a_t = a_t - a_{t-1}$  and  $\alpha_t$  is the angular acceleration derived from  $\omega_t$  (see Eq. 2).

The per-step reward used by SAC is

$$r_t = w_{\text{ctr}} r_{\text{ctr}}(t) + w_{\text{clr}} r_{\text{clr}}(t) + w_{\text{comf}} r_{\text{comf}}(t)$$
 (9)

**SAC target on the prefix.** The above equation defines the SAC target used for updating the critic during prefix fine-tuning.

$$y_t = r_t + \gamma \mathbb{E}_{A' \sim \pi_{\phi}(\cdot \mid \operatorname{ctx}_{t+1})} \left[ \min_{i \in \{1,2\}} \bar{Q}_{\bar{\theta}_i}(\operatorname{ctx}_{t+1}, A') - \alpha \log \pi_{\phi}(A' \mid \operatorname{ctx}_{t+1}) \right].$$
(10)

where  $A' \sim \pi_{\phi}(\cdot \mid \operatorname{ctx}_{t+1})$  is the next-step policy action used for bootstrapping,  $\bar{Q}_{\bar{\theta}_i}$  are target critics,  $\gamma \in (0,1)$  is the discount, and  $\alpha \geq 0$  is a fixed entropy weight.

**Critic.** We use a soft Bellman target  $y_t$  (SAC) with clipped double-Q and a conservative regularizer (CQL) to regress twin critics:

$$\mathcal{L}_{\text{critic}} = \frac{1}{2} \sum_{i=1}^{2} \left( Q_{\theta_i}(\text{ctx}_t, A_t) - y_t \right)^2$$

$$+ \alpha_{\text{cql}} \sum_{i=1}^{2} \left[ \log \sum_{a} e^{Q_{\theta_i}(\text{ctx}_t, a)} - Q_{\theta_i}(\text{ctx}_t, A_t) \right].$$
(11)

where  $Q_{\theta_i}$  are trainable twin critics and  $\alpha_{\rm cql} \geq 0$  controls the conservative penalty that down-weights OOD actions.

**Actor.** The policy minimizes the KL divergence to the Boltzmann distribution induced by Q (discrete actions use exact summation):

$$\mathcal{L}_{actor} = \mathbb{E}_{ctx} \left[ \alpha \sum_{a} \pi_{\phi}(a \mid ctx) \log \pi_{\phi}(a \mid ctx) - \sum_{a} \pi_{\phi}(a \mid ctx) \min_{i} Q_{\theta_{i}}(ctx, a) \right].$$
 (12)

**SAC loss.** The final SAC objective combines the critic regression and actor policy terms with tunable weights, as shown below.

$$\mathcal{L}_{SAC} = \lambda_{critic} \, \mathcal{L}_{critic} + \lambda_{actor} \, \mathcal{L}_{actor}$$
 (13)

Behavior cloning (value-aware). This objective performs value-aware behavior cloning: the critic-derived advantage  $(Adv_t)$  compares the expert action value against the policy's value baseline, and the exponential weight  $(w_t)$  (AWAC-style) upweights high-advantage expert actions in the BC loss, biasing imitation toward actions that are not only likely but also value-improving.

$$Adv_t = \min_i Q_{\theta_i}(\operatorname{ctx}_t, A_t^{\mathsf{gt}})$$
$$-\sum_{a=0}^{A-1} \pi_{\phi}(a \mid \operatorname{ctx}_t) \min_i Q_{\theta_i}(\operatorname{ctx}_t, a), \qquad (14)$$

$$\mathcal{L}_{BC} = \mathbb{E}\left[w_t \cdot \left(-\log \pi_{\phi}(A_t^{\text{gt}} \mid \text{ctx}_t)\right)\right]. \tag{15}$$

where  $A_t^{\rm gt}$  is the expert action token at step t,  $w_t = \exp({\rm Adv}_t/\lambda_{\rm awac})$  is the AWAC weight with temperature  $\lambda_{\rm awac} > 0$ , and  $\pi_\phi(\cdot \mid {\rm ctx}_t)$  is the discrete policy over the trajectory-token vocabulary.

**Total objective.** We optimize a weighted sum of the SAC and BC objectives, with  $\lambda$  controlling the BC weight.

$$\mathcal{L}_{total} = \mathcal{L}_{SAC} + \lambda \mathcal{L}_{BC}$$

Combined with former IL process, our two-stage training process is shown in Figure 4: (I) behavior cloning pretrains a strong perception-to-plan prior over discrete BEV and  $\kappa$ -a tokens; (II) offline SAC-BC then *breaks the loss symmetry* by optimizing explicit rewards (safety distance, comfort, progress) while regularizing toward the BC policy. This shifts learning from mere label matching to risk-aware selection, e.g., preferring the left trajectory in Fig. 3 rather then the right one.

#### 3.3. Trajectory Post-tuning

The discrete  $\kappa$ -a tokenization is compact and robust but may miss small displacements and induce abrupt token switches, occasionally manifesting as lateral zig-zag or comfort degradation. To mitigate these flaws, we introduce a lightweight post-tuning stage that refines the predicted trajectory using BEV lane evidence and finite-difference regularization.

**Formulation.** Given the predicted waypoints  $\{(x_t, y_t, \psi_t)\}_{t=1}^H$  and a lane-center likelihood map  $P \in [0, 1]^{H \times W}$ , we first obtain lane anchors  $(x_t^{\text{lane}}, y_t^{\text{lane}})$  by gradient ascent on P. In the local Frenet frame  $(s_t, \ell_t)$ , we minimize a regularized least-squares objective:

$$\min_{\Delta \ell} \|\Delta \ell - (\ell^{\text{lane}} - \ell)\|_{2}^{2} + w_{\ell,1} \|D_{1} \Delta \ell\|_{2}^{2} + w_{\ell,2} \|D_{2} \Delta \ell\|_{2}^{2},$$
(16)

where  $D_1, D_2$  are first/second-order finite-difference operators. A similar 1D smoothing is applied longitudinally:

$$\min_{\mathbf{s}} \|\mathbf{s} - \mathbf{s}_{\text{raw}}\|_{2}^{2} + w_{s,1} \|D_{1}\mathbf{s}\|_{2}^{2} + w_{s,2} \|D_{2}\mathbf{s}\|_{2}^{2}.$$
 (17)

Finally, yaw angles are recomputed from the refined  $(x_t,y_t)$  and softly smoothed under a per-step rate limit.

This optimization preserves the planner's intent while aligning the trajectory with lane geometry and enforcing local smoothness, yielding improved feasibility and ride comfort without introducing new learnable modules.

# 4. Experiments

### 4.1. Implementation Details

We train on NavSim [10] at 2 Hz with a two-stage schedule: the first 4 epochs use pure behavioral cloning to stabilize representations and align with teacher trajectories, followed by a second stage that optimizes the full objective for a total of 16 epochs; optimization uses AdamW (lr  $1 \times 10^{-4}$ , weight decay  $1 \times 10^{-4}$ ), gradient clipping at 1.0, and  $n_{\rm step}{=}3$  rollout steps per update, with runs on  $4\times A800$  (80 GB) and effective batch size scaled with device count. For nuScenes [2] evaluation, we train a separate model using only the BC stage. Images and LiDAR are rasterized into BEV using the TransFuser [8] pipeline; a pretrained  $\sim 50$ M-parameter TransFuser encoder with a ResNet-34 backbone fuses modalities and produces semantic BEV maps, which feed our planning transformer.

#### 4.2. Open-loop Evaluation

We conduct open-loop evaluations on nuScenes [2] and NuPlan [3]. On nuScenes, following UniAD and ST-P3 we report  $L2_{\rm max}$  and  $L2_{\rm avg}$ ; to avoid cross-domain leakage, our nuScenes model is trained with imitation learning only (BC stage). Under the same IL protocol, we only compare against MiMo-VL-7B-SFT rather than its MAX-V1 variants (which rely on extra RL). Our planner attains the best  $L2_{\rm max}$  and matches the top  $L2_{\rm avg}$ , evidencing stronger worst-case control without eroding average error.

On NuPlan, we use the full Nuplan mini set for training and evaluate on Val4k, Test4k, and Val14 following STR2-CKS [38]. As summarized in Table 2, DAP sets a new state of the art on 8s ADE and OLS across all three splits (e.g., Val4k: 1.202 ADE, 91.68% OLS), while remaining competitive on 8s FDE—slightly above PlanTF on Test4k/Val14 yet substantially ahead of other SOTA baselines overall. The pattern is consistent: DAP improves distribution-level accuracy and reliability (ADE/OLS) and preserves strong final-step precision without resorting to task-specific tuning or additional modalities.

Table 1. Main results on nuScenes. No extra information beyond sensors unless noted.  $L2_{\rm max}$  from UniAD and  $L2_{\rm avg}$  from ST-P3. "Avg." averages the first three seconds.

Model		$\mathbf{L2}_{\mathrm{avg}}$	(m) ↓	$\mathbf{L2_{\mathrm{max}}}$ (m) $\downarrow$				
Model	1s	2s	3s	Avg.	1s	2s	3s	Avg.
VAD [17]	0.41	0.70	1.05	0.72	_	-	-	_
BridgeAD [47]	0.28	0.55	0.92	0.58	_	_	_	_
UniAD [13]	0.42	0.64	0.91	0.66	0.48	0.96	1.65	1.03
SparseDrive [39]	0.29	0.58	0.96	0.61	_	_	_	_
SSR [22]	0.19	0.36	0.62	0.39	0.25	0.64	1.33	0.74
OpenDriveVLA [49]	0.15	0.31	0.55	0.33	0.20	0.58	1.21	0.66
EMMA* [16]	0.14	0.29	0.54	0.32	_	_	_	_
EMMA+* [16]	0.13	0.27	0.48	0.29	-	_	_	_
MAX-V1* [46]	0.24	0.38	0.65	0.42	0.28	0.63	1.41	0.77
Ours (DAP)	0.17	0.33	0.52	0.34	0.24	0.58	1.06	0.63

Note: \* additional model details: EMMA is initialized from Google Gemini [16]; EMMA+ is pre-trained on Waymo's internal extra data. For MAX-V1, we show results of MiMo-VL-7B-SFT. **Bold** indicates the best result, and <u>underline</u> indicates the second best.

Table 2. Performance on NuPlan open-loop metrics, compared with various state-of-the-art models. Lower is better for 8s-ADE/8s-FDE (m); higher is better for OLS (%).

Method	Val4k Set			Test4k Set			Val14 Set		
	8sADE ↓	8sFDE ↓	OLS ↑	8sADE ↓	8sFDE ↓	OLS ↑	8sADE ↓	8sFDE ↓	OLS ↑
PlanCNN [32]	_	_	_	_	_	_	2.468	5.936	64
PDM-Hybrid [9]	2.435	5.202	84.06	2.618	5.546	82.04	2.381	5.068	84
PlanTF [6]	1.774	3.892	88.59	1.855	4.042	87.30	1.697	3.714	89.18
DTPP [15]	4.196	9.231	65.15	4.117	9.181	64.18	4.088	8.846	67.33
STR2-CKS-800m [38]	1.473	4.124	90.07	1.537	4.269	89.12	1.496	4.219	89.2
Ours (DAP)	1.202	3.711	91.68	1.393	4.090	90.16	1.311	3.942	91.02

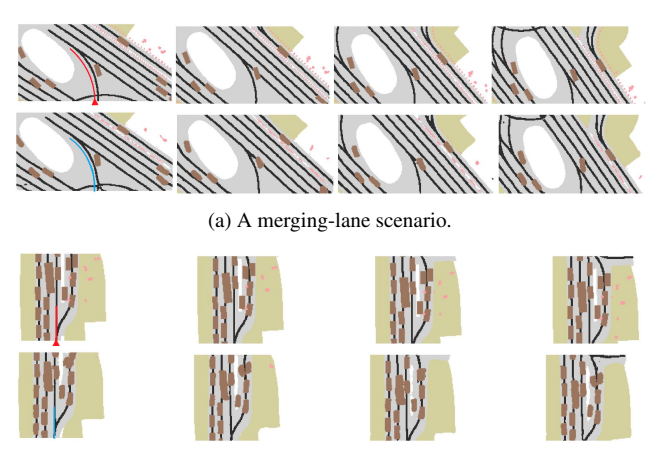
Note: Bold indicates the best result.

## 4.3. Closed-loop Evaluation on NavSim

We follow the official NavSim [10] v1 Predictive Driver Model Score (PDMS), which gates progress terms by safety compliance and averages weighted drivability terms; all subscores are simulator-derived and normalized to [0,1], and PDMS is computed as PDMS = NC · DAC ·  $\frac{5 \, \text{EP} + 5 \, \text{TTC} + 2 \, \text{C}}{12}$ . The results are shown in Table 3. Though the efficient 160M model makes it among the most lightweight planners, **DAP** delivers a competitive PDMS of 87.2, with perfect comfort (C=100.0) and strong safety margins (TTC=96.5), whereas many recent approaches with higher PDMS (e.g., driveVAL-W0) rely on VLM backbones with billions of parameters.

## 4.4. Qualitative Results

In this section, we provide qualitative visualizations in Figure 5. Our planner **DAP** *jointly* predicts future BEV semantics and ego trajectories, enabling the planner to reason about scene context and motion in a tightly coupled fashion. Subfigure (a) depicts a merging-lane scenario, while subfigure (b) illustrates a case with dense leading traffic. In each subfigure, the top row shows the ground-truth ego trajectory and future three-frame BEV semantics, whereas the bottom row presents our predicted trajectory and BEV scene. For a fair and intuitive comparison, the trajectories in the leftmost column of each panel are rendered on the same ground-truth BEV background. As shown in the figure, our model not only generates highly accurate trajectory plans, but also produces precise forecasts of the future BEV



(b) Scenario with dense leading traffic.

Figure 5. Qualitative comparison of jointly forecasted BEV semantics and ego trajectories (bottom rows) against ground truth (top rows).

scene, demonstrating strong consistency between the predicted environment representation and the planned motion.

#### 4.5. Ablation Study

Ablation on trajectory discretization. We compare fixed-bin discretization (FB) on xy and curvature–acceleration  $(\kappa-a)$ , IBQ [37] (xy and  $\kappa-a$ ), and DCT (xy and  $\kappa-a$ ). As shown in Table 4, DCT attains the smallest open-loop errors but relies on global bases: each token encodes a long temporal segment, which couples distant steps and interacts poorly with autoregressive rollout, making credit assignment and local edits difficult. In contrast, ka-FB operates

Table 3. Closed-loop performance on PDMS. Higher is better ( $\uparrow$ ). **Bold** is best in each block. C denotes camera-only inputs, while L indicates the inclusion of LiDAR in addition to cameras.

Method	Ref	Sensors	NC↑	DAC↑	TTC↑	<b>C.</b> ↑	EP↑	PDMS↑
Human	_	_	100	100	100	99.9	87.5	94.8
UniAD [13]	CVPR'23	С	97.8	91.9	92.9	100.0	78.8	83.4
TransFuser [8]	TPAMI'23	C + L	97.7	92.8	92.8	100.0	79.2	84.0
PARA-Drive [43]	CVPR'24	C	97.9	92.4	93.0	99.8	79.3	84.0
Hydra-MDP [28]	arXiv'24	C + L	98.3	96.0	96.4	100.0	78.7	86.5
DiffusionDrive [29]	CVPR'25	C + L	98.2	96.2	94.7	100.0	82.2	88.1
WoTE [26]	ICCV'25	C+L	98.5	96.8	94.4	99.9	81.9	88.3
AutoVLA [50]	NeurIPS'25	С	98.4	95.6	98.0	99.9	81.9	89.1
ReCogDrive [27]	arXiv'25	C	98.2	97.8	95.2	99.8	83.5	89.6
DriveVLA-W0* [25]	arXiv'25	C	98.7	99.1	95.3	99.3	83.3	90.2
Ours (DAP)	-	C+L	95.2	97.4	96.5	100.0	82.2	87.2

Table 4. Ablation study on trajectory discretization.

Method	Nuplan	mini [3]	Nusce	nes [2]	Navsim [10]	
	4sADE ↓	4sFDE ↓	4sADE ↓	4sFDE ↓	4sADE ↓	4sFDE ↓
xy-FB [21]	*	*	*	*	*	*
ka-FB	0.40	0.68	0.55	1.02	0.33	0.68
xy-IBQ	0.71	1.67	_	_	1.18	3.90
ka-IBQ	0.42	1.40	2.84	6.38	1.32	2.77
xy-DCT [31]	0.26	0.32	0.29	0.39	0.42	0.58
ka-DCT	0.35	1.10	0.30	0.88	0.30	0.96

Note: \* denotes resolution-limited results: for uniform bin size  $\Delta$ , the quantization error scales linearly as  $O(\Delta)$  and is bounded by  $\leq \Delta/2$  per axis (e.g.,  $\Delta=0.5$  m  $\Rightarrow$  error <0.25 m).

Table 5. Ablation study for model in training and inference.

Model	NAVSIM v1							
	NC↑	DAC↑	TTC↑	C.↑	EP↑	PDMS↑		
Planner(only traj tokens)	94.2	92.9	95.0	98.8	84.26	82.7		
DAP (only BC)	94.6	94.1	94.6	98.9	90.2	84.6		
DAP (SACBC)	97.4	94.8	97.4	98.7	87.8	87.0		
DAP (post-tuning)	95.2	97.4	96.5	1.00	82.2	87.2		

in a behavior-aligned space (steering curvature and longitudinal acceleration), achieving competitive or better errors with a vocabulary roughly an order of magnitude smaller than xy-FB and DCT (excluding IBQ). This compactness improves sampling efficiency and coverage of rare maneuvers. IBQ performs worse here because the trajectory space is intrinsically low-dimensional and information-sparse, so the learned codebook tends to collapse toward frequent patterns and fails to faithfully represent rare, sharp maneuvers. We therefore adopt **ka-FB** as our default discretization. A remaining caveat is the reconstruction bias between ka and xy representations, which is small in practice but still a target for future refinement.

**Ablation on interface and training regime.** We first ablate the supervision interface by removing the BEV head ("only trajectory tokens," no BEV tokens are produced during training and inference). This variant yields the weakest composite performance (PDMS=82.7). Restoring the joint BEV-trajectory interface under pure BC maximizes progress (EP=90.2) yet leaves safety suboptimal (PDMS=84.6). Introducing SAC-BC markedly strengthens safety and reactivity (NC=97.4, TTC=97.4) and improves

the overall score to PDMS=87.0 with a modest reduction in EP (87.8). A lightweight post-tuning stage further regularizes driving priors, delivering the best drivable-area compliance and comfort (DAC=97.4, C=1.00) and the highest final score (PDMS=87.2), despite a larger progress drop (EP=82.2). Overall, (i) joint BEV and trajectory supervision outperforms trajectory-only training, (ii) SAC-BC enhances environment understanding and ego-scene interaction, and (iii) post-tuning slightly trades progress for higher compliance and comfort, yielding the best overall performance.

#### 5. Conclusion

In this work, we claim that discrete-token, decoder-only autoregression is a promising and scalable paradigm for motion planning. We introduce **DAP**, a discrete-token autoregressive planner that jointly forecasts future BEV semantics and trajectory tokens, supplying dense, spatiotemporally aligned supervision that tightly couples scene understanding with motion generation. On this foundation, we add SAC-BC fine-tuning to inject reward-driven adaptation without altering the autoregressive pattern, yielding substaintial gains in closed-loop interaction. Despite a compact 160M model size, DAP attains state-of-the-art openloop metrics and strong closed-loop performance, indicating that discrete-token autoregression offers a simple yet powerful recipe, one that scales gracefully and bridges imitation and reinforcement toward more general driving intelligence.

#### References

- [1] Mustafa Baniodeh, Kratarth Goel, Scott Ettinger, Carlos Fuertes, Ari Seff, Tim Shen, Cole Gulino, Chenjie Yang, Ghassen Jerfel, Dokook Choe, et al. Scaling laws of motion forecasting and planning—a technical report. arXiv preprint arXiv:2506.08228, 2025. 2
- [2] Holger Caesar, Varun Bankiti, Alex H Lang, Sourabh Vora, Venice Erin Liong, Qiang Xu, Anush Krishnan, Yu Pan, Giancarlo Baldan, and Oscar Beijbom. nuscenes: A multimodal dataset for autonomous driving. In *Proceedings of* the IEEE/CVF conference on computer vision and pattern recognition, pages 11621–11631, 2020. 6, 8
- [3] Holger Caesar, Juraj Kabzan, Kok Seang Tan, Whye Kit Fong, Eric Wolff, Alex Lang, Luke Fletcher, Oscar Beijbom, and Sammy Omari. nuplan: A closed-loop ml-based planning benchmark for autonomous vehicles. *arXiv preprint arXiv:2106.11810*, 2021. 6, 8
- [4] Jun Cen, Chaohui Yu, Hangjie Yuan, Yuming Jiang, Siteng Huang, Jiayan Guo, Xin Li, Yibing Song, Hao Luo, Fan Wang, Deli Zhao, and Hao Chen. Worldvla: Towards autoregressive action world model, 2025.
- [5] Shaoyu Chen, Bo Jiang, Hao Gao, Bencheng Liao, Qing Xu, Qian Zhang, Chang Huang, Wenyu Liu, and Xinggang Wang. Vadv2: End-to-end vectorized autonomous driving via probabilistic planning. arXiv preprint arXiv:2402.13243, 2024. 2
- [6] Jie Cheng, Yingbing Chen, Xiaodong Mei, Bowen Yang, Bo Li, and Ming Liu. Rethinking imitation-based planners for autonomous driving. In 2024 IEEE International Conference on Robotics and Automation (ICRA), pages 14123–14130. IEEE, 2024. 7
- [7] Pengyu Cheng, Yifan Yang, Jian Li, Yong Dai, and Nan Du. Adversarial preference optimization. *CoRR*, 2023. 3
- [8] Kashyap Chitta, Aditya Prakash, Bernhard Jaeger, Zehao Yu, Katrin Renz, and Andreas Geiger. Transfuser: Imitation with transformer-based sensor fusion for autonomous driving. *IEEE transactions on pattern analysis and machine in*telligence, 45(11):12878–12895, 2022. 6, 8
- [9] Daniel Dauner, Marcel Hallgarten, Andreas Geiger, and Kashyap Chitta. Parting with misconceptions about learningbased vehicle motion planning. In *Conference on Robot Learning*, pages 1268–1281. PMLR, 2023. 7
- [10] Daniel Dauner, Marcel Hallgarten, Tianyu Li, Xinshuo Weng, Zhiyu Huang, Zetong Yang, Hongyang Li, Igor Gilitschenski, Boris Ivanovic, Marco Pavone, et al. Navsim: Data-driven non-reactive autonomous vehicle simulation and benchmarking. Advances in Neural Information Processing Systems, 37:28706–28719, 2024. 6, 7, 8
- [11] Renju Feng, Ning Xi, Duanfeng Chu, Rukang Wang, Zejian Deng, Anzheng Wang, Liping Lu, Jinxiang Wang, and Yanjun Huang. Artemis: Autoregressive end-to-end trajectory planning with mixture of experts for autonomous driving, 2025. 1, 2
- [12] Jordan Hoffmann, Sebastian Borgeaud, Arthur Mensch, Elena Buchatskaya, Trevor Cai, Eliza Rutherford, Diego de Las Casas, Lisa Anne Hendricks, Johannes Welbl, Aidan Clark, Tom Hennigan, Eric Noland, Katie Millican, George

- van den Driessche, Bogdan Damoc, Aurelia Guy, Simon Osindero, Karen Simonyan, Erich Elsen, Jack W. Rae, Oriol Vinyals, and Laurent Sifre. Training compute-optimal large language models, 2022. 1
- [13] Yihan Hu, Jiazhi Yang, Li Chen, Keyu Li, Chonghao Sima, Xizhou Zhu, Siqi Chai, Senyao Du, Tianwei Lin, Wenhai Wang, et al. Planning-oriented autonomous driving. In Proceedings of the IEEE/CVF conference on computer vision and pattern recognition, pages 17853–17862, 2023. 2, 7, 8
- [14] Xin Huang, Eric M. Wolff, Paul Vernaza, Tung Phan-Minh, Hongge Chen, David S. Hayden, Mark Edmonds, Brian Pierce, Xinxin Chen, Pratik Elias Jacob, Xiaobai Chen, Chingiz Tairbekov, Pratik Agarwal, Tianshi Gao, Yuning Chai, and Siddhartha Srinivasa. Drivegpt: Scaling autoregressive behavior models for driving, 2025. 1, 2
- [15] Zhiyu Huang, Peter Karkus, Boris Ivanovic, Yuxiao Chen, Marco Pavone, and Chen Lv. Dtpp: Differentiable joint conditional prediction and cost evaluation for tree policy planning in autonomous driving. In 2024 IEEE International Conference on Robotics and Automation (ICRA), pages 6806–6812. IEEE, 2024. 7
- [16] Jyh-Jing Hwang, Runsheng Xu, Hubert Lin, Wei-Chih Hung, Jingwei Ji, Kristy Choi, Di Huang, Tong He, Paul Covington, Benjamin Sapp, et al. Emma: End-to-end multimodal model for autonomous driving. arXiv preprint arXiv:2410.23262, 2024. 7
- [17] Bo Jiang, Shaoyu Chen, Qing Xu, Bencheng Liao, Jiajie Chen, Helong Zhou, Qian Zhang, Wenyu Liu, Chang Huang, and Xinggang Wang. Vad: Vectorized scene representation for efficient autonomous driving. In *Proceedings of the IEEE/CVF International Conference on Computer Vision*, pages 8340–8350, 2023. 7
- [18] Xuefeng Jiang, Yuan Ma, Pengxiang Li, Leimeng Xu, Xin Wen, Kun Zhan, Zhongpu Xia, Peng Jia, Xianpeng Lang, and Sheng Sun. Transdiffuser: Diverse trajectory generation with decorrelated multi-modal representation for end-to-end autonomous driving, 2025.
- [19] Siwen Jiao, Kangan Qian, Hao Ye, Yang Zhong, Ziang Luo, Sicong Jiang, Zilin Huang, Yangyi Fang, Jinyu Miao, Zheng Fu, Yunlong Wang, Kun Jiang, Diange Yang, Rui Fan, and Baoyun Peng. Evadrive: Evolutionary adversarial policy optimization for end-to-end autonomous driving, 2025. 1, 3
- [20] Jared Kaplan, Sam McCandlish, Tom Henighan, Tom B. Brown, Benjamin Chess, Rewon Child, Scott Gray, Alec Radford, Jeffrey Wu, and Dario Amodei. Scaling laws for neural language models, 2020. 1
- [21] Moo Jin Kim, Karl Pertsch, Siddharth Karamcheti, Ted Xiao, Ashwin Balakrishna, Suraj Nair, Rafael Rafailov, Ethan Foster, Grace Lam, Pannag Sanketi, et al. Openvla: An open-source vision-language-action model, 2024. URL https://arxiv. org/abs/2406.09246, 2024. 8
- [22] Peidong Li and Dixiao Cui. Does end-to-end autonomous driving really need perception tasks? arXiv e-prints, pages arXiv-2409, 2024. 7
- [23] Shuang Li, Yihuai Gao, Dorsa Sadigh, and Shuran Song. Unified video action model, 2025.
- [24] Yingyan Li, Lue Fan, Jiawei He, Yuqi Wang, Yuntao Chen, Zhaoxiang Zhang, and Tieniu Tan. Enhancing end-to-

- end autonomous driving with latent world model. In *International Conference on Representation Learning*, pages 42942–42959, 2025. 2
- [25] Yingyan Li, Shuyao Shang, Weisong Liu, Bing Zhan, Haochen Wang, Yuqi Wang, Yuntao Chen, Xiaoman Wang, Yasong An, Chufeng Tang, et al. Drivevla-w0: World models amplify data scaling law in autonomous driving. arXiv preprint arXiv:2510.12796, 2025. 2, 8
- [26] Yingyan Li, Yuqi Wang, Yang Liu, Jiawei He, Lue Fan, and Zhaoxiang Zhang. End-to-end driving with online trajectory evaluation via bev world model. *arXiv preprint* arXiv:2504.01941, 2025. 8
- [27] Yongkang Li, Kaixin Xiong, Xiangyu Guo, Fang Li, Sixu Yan, Gangwei Xu, Lijun Zhou, Long Chen, Haiyang Sun, Bing Wang, Kun Ma, Guang Chen, Hangjun Ye, Wenyu Liu, and Xinggang Wang. Recogdrive: A reinforced cognitive framework for end-to-end autonomous driving, 2025. 3, 8
- [28] Zhenxin Li, Kailin Li, Shihao Wang, Shiyi Lan, Zhiding Yu, Yishen Ji, Zhiqi Li, Ziyue Zhu, Jan Kautz, Zuxuan Wu, et al. Hydra-mdp: End-to-end multimodal planning with multitarget hydra-distillation. arXiv preprint arXiv:2406.06978, 2024. 1, 8
- [29] Bencheng Liao, Shaoyu Chen, Haoran Yin, Bo Jiang, Cheng Wang, Sixu Yan, Xinbang Zhang, Xiangyu Li, Ying Zhang, Qian Zhang, et al. Diffusiondrive: Truncated diffusion model for end-to-end autonomous driving. In *Proceedings of the Computer Vision and Pattern Recognition Conference*, pages 12037–12047, 2025. 1, 8
- [30] Yiren Lu, Justin Fu, George Tucker, Xinlei Pan, Eli Bronstein, Rebecca Roelofs, Benjamin Sapp, Brandyn White, Aleksandra Faust, Shimon Whiteson, et al. Imitation is not enough: Robustifying imitation with reinforcement learning for challenging driving scenarios. In 2023 IEEE/RSJ International Conference on Intelligent Robots and Systems (IROS), pages 7553–7560. IEEE, 2023. 2, 3, 5
- [31] Karl Pertsch, Kyle Stachowicz, Brian Ichter, Danny Driess, Suraj Nair, Quan Vuong, Oier Mees, Chelsea Finn, and Sergey Levine. Fast: Efficient action tokenization for visionlanguage-action models. arXiv preprint arXiv:2501.09747, 2025. 8
- [32] Katrin Renz, Kashyap Chitta, Otniel-Bogdan Mercea, A Koepke, Zeynep Akata, and Andreas Geiger. Plant: Explainable planning transformers via object-level representations. arXiv preprint arXiv:2210.14222, 2022. 7
- [33] John Schulman, Yan Duan, Jonathan Ho, Alex Lee, Ibrahim Awwal, Henry Bradlow, Jia Pan, Sachin Patil, Ken Goldberg, and Pieter Abbeel. Motion planning with sequential convex optimization and convex collision checking. *The In*ternational Journal of Robotics Research, 33(9):1251–1270, 2014. 3
- [34] Ari Seff, Brian Cera, Dian Chen, Mason Ng, Aurick Zhou, Nigamaa Nayakanti, Khaled S Refaat, Rami Al-Rfou, and Benjamin Sapp. Motionlm: Multi-agent motion forecasting as language modeling. In Proceedings of the IEEE/CVF International Conference on Computer Vision, pages 8579– 8590, 2023. 1
- [35] Hao Shao, Letian Wang, Ruobing Chen, Hongsheng Li, and Yu Liu. Safety-enhanced autonomous driving using inter-

- pretable sensor fusion transformer. In *Conference on Robot Learning*, pages 726–737. PMLR, 2023. 3
- [36] Zhihong Shao, Peiyi Wang, Qihao Zhu, Runxin Xu, Junxiao Song, Xiao Bi, Haowei Zhang, Mingchuan Zhang, YK Li, Yang Wu, et al. Deepseekmath: Pushing the limits of mathematical reasoning in open language models. *arXiv preprint arXiv:2402.03300*, 2024. 3
- [37] Fengyuan Shi, Zhuoyan Luo, Yixiao Ge, Yujiu Yang, Ying Shan, and Limin Wang. Taming scalable visual tokenizer for autoregressive image generation. *arXiv e-prints*, pages arXiv–2412, 2024. 7
- [38] Qiao Sun, Huimin Wang, Jiahao Zhan, Fan Nie, Xin Wen, Leimeng Xu, Kun Zhan, Peng Jia, Xianpeng Lang, and Hang Zhao. Generalizing motion planners with mixture of experts for autonomous driving, 2024. 2, 6, 7
- [39] Wenchao Sun, Xuewu Lin, Yining Shi, Chuang Zhang, Haoran Wu, and Sifa Zheng. Sparsedrive: End-to-end autonomous driving via sparse scene representation. In 2025 IEEE International Conference on Robotics and Automation (ICRA), pages 8795–8801. IEEE, 2025. 7
- [40] Aaron van den Oord, Oriol Vinyals, and koray kavukcuoglu. Neural discrete representation learning. In Advances in Neural Information Processing Systems. Curran Associates, Inc., 2017.
- [41] Matt Vitelli, Yan Chang, Yawei Ye, Ana Ferreira, Maciej Wołczyk, Błażej Osiński, Moritz Niendorf, Hugo Grimmett, Qiangui Huang, Ashesh Jain, and Peter Ondruska. Safetynet: Safe planning for real-world self-driving vehicles using machine-learned policies. In 2022 International Conference on Robotics and Automation (ICRA), pages 897–904, 2022. 3
- [42] Yuqi Wang, Xinghang Li, Wenxuan Wang, Junbo Zhang, Yingyan Li, Yuntao Chen, Xinlong Wang, and Zhaoxiang Zhang. Unified vision-language-action model, 2025. 4
- [43] Xinshuo Weng, Boris Ivanovic, Yan Wang, Yue Wang, and Marco Pavone. Para-drive: Parallelized architecture for realtime autonomous driving. In *Proceedings of the IEEE/CVF* Conference on Computer Vision and Pattern Recognition, pages 15449–15458, 2024. 8
- [44] Yanhao Wu, Haoyang Zhang, Tianwei Lin, Lichao Huang, Shujie Luo, Rui Wu, Congpei Qiu, Wei Ke, and Tong Zhang. Generating multimodal driving scenes via next-scene prediction, 2025.
- [45] Zhenhua Xu, Yujia Zhang, Enze Xie, Zhen Zhao, Yong Guo, Kwan-Yee. K. Wong, Zhenguo Li, and Hengshuang Zhao. Drivegpt4: Interpretable end-to-end autonomous driving via large language model, 2024.
- [46] Sheng Yang, Tong Zhan, Guancheng Chen, Yanfeng Lu, and Jian Wang. Less is more: Lean yet powerful visionlanguage model for autonomous driving. arXiv preprint arXiv:2510.00060, 2025. 7
- [47] Bozhou Zhang, Nan Song, Xin Jin, and Li Zhang. Bridging past and future: End-to-end autonomous driving with historical prediction and planning. In *Proceedings of the Computer Vision and Pattern Recognition Conference*, pages 6854–6863, 2025. 7

- [48] Dongkun Zhang, Jiaming Liang, Ke Guo, Sha Lu, Qi Wang, Rong Xiong, Zhenwei Miao, and Yue Wang. Carplanner: Consistent auto-regressive trajectory planning for largescale reinforcement learning in autonomous driving. In 2025 IEEE/CVF Conference on Computer Vision and Pattern Recognition (CVPR), pages 17239–17248, 2025. 1, 2
- [49] Xingcheng Zhou, Xuyuan Han, Feng Yang, Yunpu Ma, and Alois C Knoll. Opendrivevla: Towards end-to-end autonomous driving with large vision language action model. arXiv preprint arXiv:2503.23463, 2025. 7
- [50] Zewei Zhou, Tianhui Cai, Seth Z Zhao, Yun Zhang, Zhiyu Huang, Bolei Zhou, and Jiaqi Ma. Autovla: A vision-language-action model for end-to-end autonomous driving with adaptive reasoning and reinforcement fine-tuning. *arXiv* preprint arXiv:2506.13757, 2025. 3, 8

# **Appendix**

#### A. More Qualitative Results

In this section, we present additional planned trajectories and future BEV semantics to further demonstrate the capability of our model, **DAP**.

#### A.1. Trajectory Visualization

In Figure 6, we visualize the predicted trajectories produced by DAP in both simple and complex urban scenarios. In each case, the red curve denotes the ground-truth ego trajectory and the blue curve indicates the corresponding planned trajectory. As shown in the simple case, our planner closely tracks the expert behavior while maintaining smooth motion and respecting lane geometry. In the more challenging scenario with multi-turn maneuvers and interactions with surrounding traffic, the predicted trajectory remains feasible and collision-free, and it anticipates future scene evolution rather than overreacting to short-term fluctuations. These qualitative results further highlight that DAP generates coherent, interpretable plans that align well with human demonstrations across diverse driving conditions.

#### A.2. BEV Visualization

In Figure 7, we provide qualitative BEV visualizations for four representative scenarios with 8 future frames. For each scenario, the top row shows the ground-truth future BEV semantics, while the bottom row presents the corresponding predictions of DAP. Overall, our model produces relatively accurate forecasts of the future scene, capturing the main road layout, drivable areas, and dominant agent motions with good temporal consistency. Although certain fine-grained details, such as small obstacles, distant pedestrians, or the precise extent of dynamic agents, may not be reconstructed perfectly, these results demonstrate that even with a relatively compact model, DAP attains a satisfactory level of BEV prediction quality for downstream planning.

#### **B.** Analysis of Trajectory Discretization

In this section, we provide a detailed analysis of the trajectory discretization schemes used in our framework and their impact on downstream planning performance. We first compare different discretization methods in terms of reconstruction error to quantify how accurately they recover continuous trajectories from discrete codes; for each variant, we also report the corresponding configuration and hyperparameters to make the comparison transparent. We then present open-loop planning metrics under each scheme to examine how these reconstruction properties translate into actual planning behavior. Finally, we summarize the key design choices across all discretization variants to facilitate reproducibility and fair comparison. All experiments in this

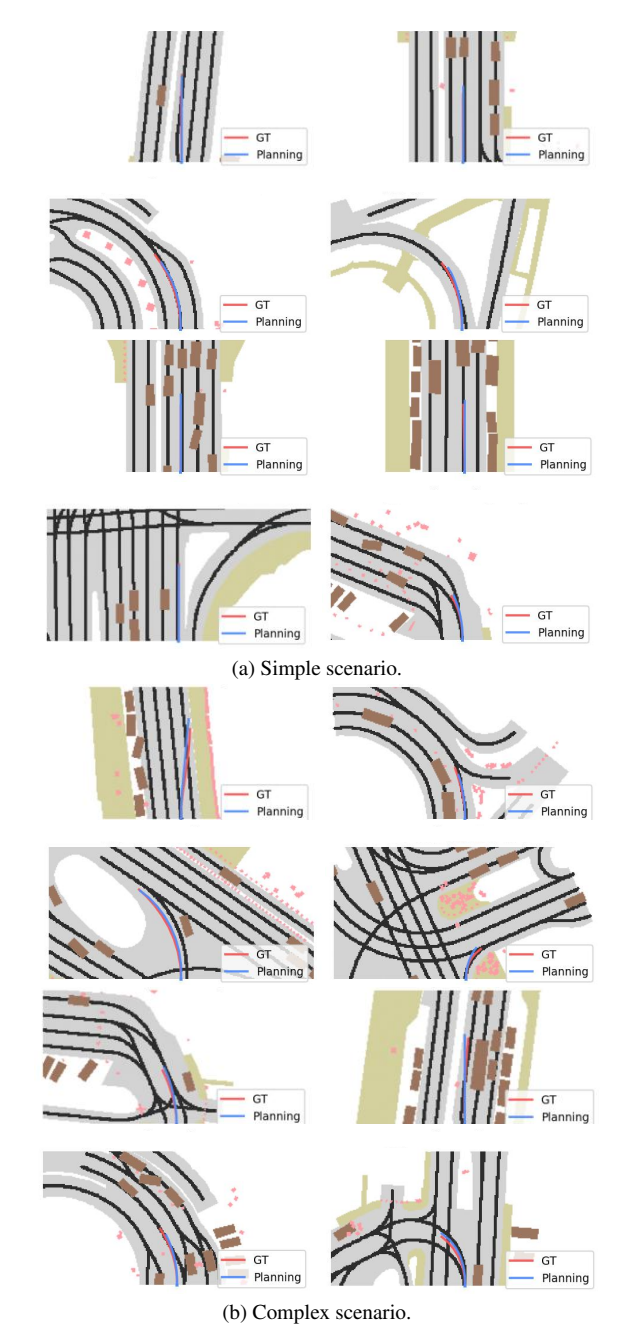


Figure 6. Qualitative trajectory visualizations in representative scenarios, where red denotes the ground-truth trajectory and blue indicates the planned trajectory.

subsection are conducted on the NuPlan-mini dataset, using a 10 Hz sampling rate with 20 past frames to predict 20 future frames.

We first report the 95% and 99% confidence intervals of the reconstruction errors for (x, y, yaw) and  $(\kappa, a)$  in Table 6. As shown, the 99% confidence intervals are markedly wider than the 95% intervals, particularly for x and a, in-

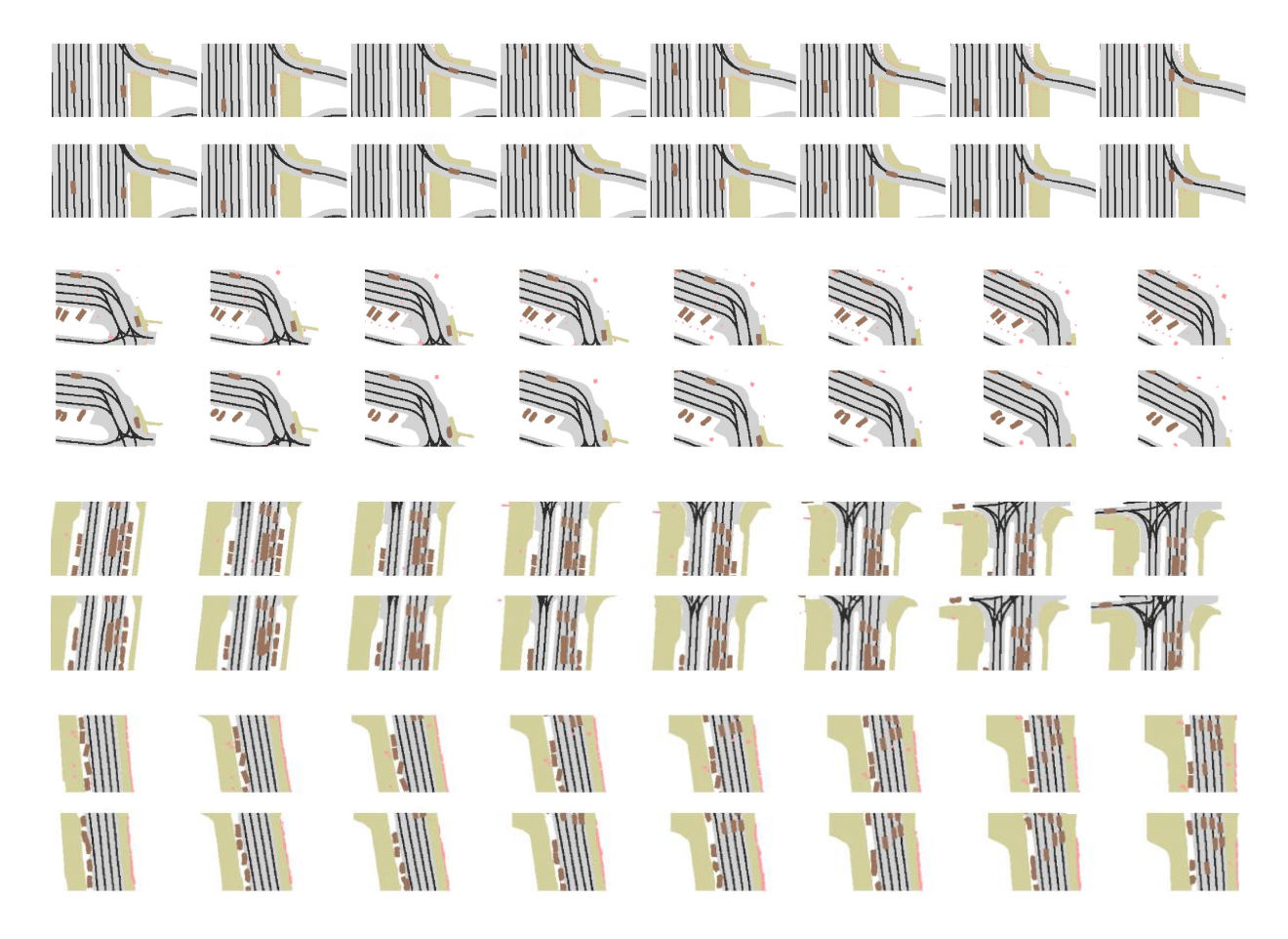


Figure 7. Qualitative BEV visualizations for four representative scenarios with 8 future frames. For each scenario, the top row shows the ground-truth future BEV semantics, and the bottom row presents the corresponding predictions of **DAP**.

dicating that under fixed-bin (FB) discretization, achieving high-coverage guarantees requires substantially larger truncation thresholds to accommodate tail reconstruction errors.

# **B.1. Comparison of Fixed-Bin and DCT Discretization**

Learning-based codebook methods such as IBQ are less attractive in our setting, because ego trajectories lie on a low-dimensional manifold with relatively simple geometric structure. In this regime, the additional parameters and training complexity of a learned quantizer offer limited gains while introducing extra sources of instability. We therefore restrict our comparison to two hand-designed

Table 6. Confidence intervals of reconstruction errors for  $(x,y,{\rm yaw})$  and  $(\kappa,a)$ .

Variable	95% CI	99% CI
x [m]	[-15.45, 16.36]	[-21.03, 22.11]
y [m]	[-0.41, 0.20]	[-1.57, 0.91]
yaw [rad]	[-0.11, 0.11]	[-0.36, 0.37]
$\kappa$	[-0.22, 0.22]	[-0.48, 0.47]
a	[-1.18, 1.31]	[-1.67, 1.86]

schemes, fixed-bin (FB) and DCT-based discretization, and empirically evaluate their behavior in terms of reconstruction error.

Table 7 reports the 4s ADE, FDE, and AHE for a range of FB and DCT configurations defined either in  $(\kappa, a)$  space or in (x, y, yaw) space. For FB schemes, the "range / step" notation denotes a uniform scalar quantizer that clips each variable to the specified interval and partitions it into equalwidth bins, e.g., the notation [-0.22; 0.01; 0.22] denotes a uniform grid from -0.22 to 0.22 with step size 0.01, resulting in 44 curvature bins. Within this family, discretizing  $(\kappa, a)$  already achieves low reconstruction error with a relatively compact codebook, whereas reaching comparable accuracy in (x, y, yaw) requires much finer spatial and yaw grids and hence a codebook that is nearly one to two orders of magnitude larger. For DCT-based schemes, we write (q, L) to indicate that each cosine coefficient is quantized with a uniform step size q and L integer levels; in our implementation, even L values produce indices in [-L/2, L/2-1], so the effective dynamic range is approximately [-(L/2)q, (L/2-1)q], e.g., q = 2.0, L = 80

Table 7. Trajectory reconstruction error under different fixed-bin (FB) and DCT discretization schemes.

Family	Config	Codebook size	$\kappa$ range and step	a range and step	(x,y) range and step	$\psi$ range and step	4s ADE (m)	4s FDE (m)	4s AHE (rad)
	A (narrow+coarse)	1146	[-0.22; 0.01; 0.22]	[-1.3; 0.10; 1.3]	-	-	0.43	1.04	0.019
FB-ka	B (wide+coarse)	3648	[-0.48; 0.01; 0.48]	[-1.9; 0.10; 1.9]	-	_	0.32	0.73	0.015
гь-ка	C (narrow+fine)	4576	[-0.22; 0.005; 0.22]	[-1.3; 0.05; 1.3]	-	_	0.31	0.70	0.008
	D (wide+fine)	14592	[-0.48; 0.005; 0.48]	[-1.9; 0.05; 1.9]	-	-	0.27	0.58	0.008
	A (narrow+coarse)	45056	_	_	[-16; 0.5; 16]	[-0.11; 0.02; 0.11]	0.49	1.60	0.009
FB-xv	B (wide+coarse)	278784	-	-	[-22; 0.5; 22]	[-0.36; 0.02; 0.36]	0.31	0.50	0.009
гь-ху	C (narrow+fine)	360448	_	-	[-16; 0.25; 16]	[-0.11; 0.01; 0.11]	0.34	1.45	0.010
	D (wide+fine)	2230272	-	-	[-22; 0.25; 22]	[-0.36; 0.01; 0.36]	0.16	0.40	0.005
DCT-xy	A (narrow)	256000	-	-	q = 2.0, L = 80	q = 0.01, L = 40	0.30	0.56	0.018
DC1-xy	B (wide)	720000	-	-	q=2.0,L=120	q = 0.01, L = 50	0.17	0.31	0.017
DCT-ka	C (narrow+coarse)	6400	q = 0.01, L = 80	q = 0.10, L = 80	_	_	0.41	0.99	0.009
DC1-Ka	D (wide+fine)	25600	q = 0.008, L = 160	q = 0.08, L = 160	-	-	0.29	0.62	0.004

Note: C denotes codebook size of trajectory token.

Table 8. Open-loop metrics for different FB-ka discretization configurations.

Method	Codebook size	2s ADE [m]	2s FDE [m]		
FB-ka-A	1146	0.45	0.69		
FB-ka-B	3648	0.42	0.63		
FB-ka-C	4576	0.44	0.64		
FB-ka-D	14592	0.61	0.97		

Note: Bold indicates the best result.

corresponds to about [-80,78]. DCT-based discretization can further reduce ADE and FDE by exploiting global temporal structure, but it relies on densely sampled trajectories over the entire horizon to compute the transform, and the resulting frequency coefficients are inherently non-local in time. As a consequence, although DCT representations provide strong reconstruction performance at the sequence level, they are poorly aligned with the notion of an instantaneous action at a single control step needed by the autoregressive structure.

# **B.2. Effect of Codebook Size on Open-Loop Performance**

In this subsection, we examine how the size of the trajectory codebook influences open-loop planning performance. To isolate this factor, we fix the BEV VQ-VAE configuration with a codebook size of 512 and use the same FB-ka discretization family for trajectories. We instantiate four FB-ka quantizers, FB-ka-A/B/C/D, which correspond to the  $(\kappa,a)$  settings analyzed in subsection B.1 and Table 7, thereby spanning a broad range of trajectory codebook sizes.

As shown in Table 8, we evaluate the 2s ADE and FDE for these four configurations. All variants share the same BEV representation and differ only in the granularity and range of the  $(\kappa, a)$  fixed-bin quantizer, which induces progressively larger trajectory codebooks from FB-ka-A to FB-ka-D. Despite the substantial change in codebook size, the open-loop errors remain relatively close, with the medium-resolution settings (FB-ka-B/C) achieving the best tradeoff, while overly narrow and coarse (A) or excessively wide and fine (D) codebooks lead to slightly degraded performance. Notably, even though the underlying trajectory re-

construction errors can be further reduced by enlarging the codebook, this does not translate into better open-loop performance of the model. This suggests that beyond a certain griding fineness, increasing trajectory codebook capacity primarily complicates optimization without yielding meaningful gains in planning quality.